

# Topological dynamics of continuum lattice structures

Yimeng Sun,<sup>1</sup> Jiacheng Xing,<sup>1</sup> Li-Hua Shao,<sup>2</sup> and Jianxiang Wang<sup>1,\*</sup>

<sup>1</sup>Department of Mechanics and Engineering Science,

College of Engineering, Peking University, Beijing 100871, China

<sup>2</sup>School of Aeronautic Science and Engineering, Beihang University, Beijing 100191, China

(Dated: August 15, 2024)

Continuum lattice structures which consist of joined elastic beams subject to flexural deformations are ubiquitous in nature and engineering. Here, first, we reveal the topological dynamics of continuous beam structures by rigorously proving the existence of infinitely many topological edge states within the bandgaps. Then, we obtain the analytical expressions for the topological phases of bulk bands, and propose a topological index related to the Zak phase that determines the existence of the edge states. The theoretical approach is directly applicable to general continuum lattice structures. We demonstrate the topological edge states of bridge-like frames, plates, and continuous beams on elastic foundations and springs, and the topological corner states of kagome frames. The continuum lattice structures serve as excellent platforms for exploring various kinds of topological phases and demonstrating the topologically protected states at multifrequencies, and their topological dynamics has significant implications in safety assessment, structural health monitoring, and energy harvesting.

*Introduction.*—Lattice structures that consist of continuum beams are ubiquitous. They are frames of large-scale structures such as buildings and bridges, skeletons of organisms [1–3], as well as small-scale advanced micro- and nanostructured materials [4–7]. Their dynamics is highly relevant to multifunctionality in wave and vibration control, safety and health monitoring [8, 9], and even to the tissue-modeling process in biology [1, 2]. The topological dynamical properties of continuum lattice structures are intriguing due to much more possibilities of topological phase transitions in continua [10], compared to the extensively investigated discrete systems [11–15]. Previous studies on topological continua usually dealt with only a few topological phase transitions in specific bandgaps, mostly based on approximate analyses and numerical calculations [16–19]. Thus, the topological dynamics of continuum lattice systems is largely unrevealed, and a theoretical framework for precisely determining the edge states at infinitely many frequencies is lacking.

In this Letter, we reveal the topological properties of a class of continuum lattice structures. Starting with the continuous beam structures, we rigorously prove the existence of infinitely many topological states within multiple bandgaps across the whole spectrum, with a clear criterion identifying the topological phase transitions. We introduce a topological index determining the edge states (instead of the interface states), which is related to the topological phases of bulk bands and a phenomenon of “eigenvalue crossing”. The theoretical framework for continuous beam structures is directly applied to reveal and demonstrate topological states in a broad range of structures including bridge-like and kagome frame structures, plate structures, and continuous beams on elastic foundations, torsional springs and linear springs.

*Topological continuous beam model on supports.*—We

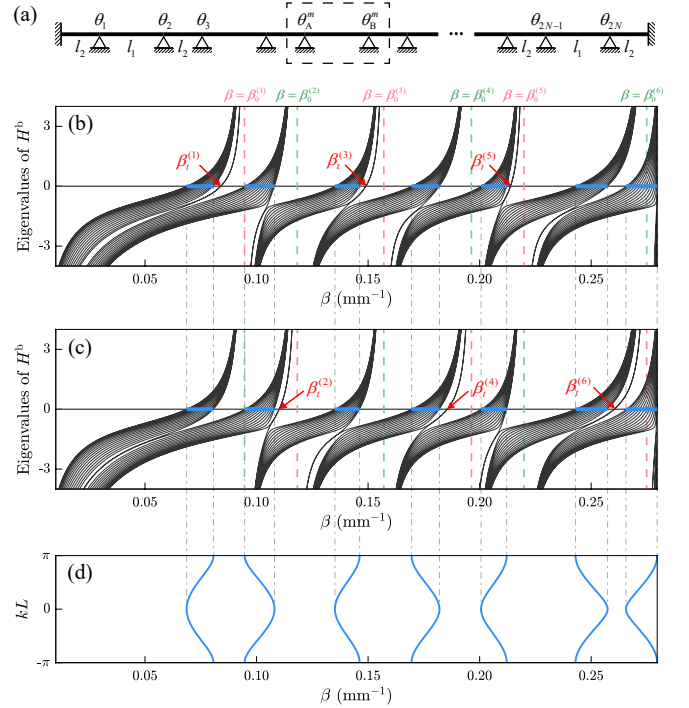


FIG. 1. (a) A continuous beam on discrete supports where a unit cell is shown in dashed frame. (b),(c) Spectra of the finite continuous beam with  $l_1 = 40$  mm,  $l_2 = 50$  mm (b), and  $l_1 = 50$  mm and  $l_2 = 40$  mm (c). Bulk bands (blue line segments), and topological edge states (red arrows). (d) Dispersion diagram of the beam with  $(l_1, l_2) = (40$  mm,  $50$  mm) and  $(50$  mm,  $40$  mm).

begin with a continuous beam model on supports, as shown in Fig. 1(a). The beam has a uniform cross-section, and it is supported on  $2N$  simple supports such that the beam has  $2N + 1$  segments with alternating lengths  $l_2, l_1, l_2, \dots, l_1, l_2$ . The two ends are clamped.

We consider the flexural motion of the continuous beam, where its deformation is described by rotations at the points of supports and deflections between the supports. The rotational angles at the supports are denoted by  $|\theta\rangle \equiv (\theta_1, \theta_2, \dots, \theta_{2N})^T$ . The deflection of the continuous beam with infinitely many degrees of freedom can be expressed via the discrete rotational angles at the supports (joints). The transverse deflection of each beam segment is taken as  $u(x, t) = \text{Re}\{\phi(x)e^{-i\omega t}\}$  ( $\omega$  represents frequency). In terms of the equation of motion of the Euler–Bernoulli beam theory,  $EI(\partial^4 u/\partial x^4) + m(\partial^2 u/\partial t^2) = 0$ , the deflection curve  $\phi(x)$  satisfies [20]

$$\phi^{(4)}(x) - \frac{\omega^2 m}{EI} \phi(x) = 0, \quad (1)$$

where  $m$  is the linear density,  $E$  is the Young modulus, and  $I$  is the moment of inertia of the cross-section. The general solution of Eq. (1) is

$$\phi(x) = C_1 \sin \beta x + C_2 \cos \beta x + C_3 \sinh \beta x + C_4 \cosh \beta x, \quad (2)$$

where  $\beta^4 = \omega^2 m/EI$  ( $\beta > 0$ ). The deflections of the beam at the joints are zero, and the rotational angles are continuous. Thus, for a generic beam segment around joint  $n \in \{1, \dots, 2N\}$  (which denotes number of the joints counting from the left), when the origin of the coordinate system is set at joint  $n$ , the deflection function  $\phi(x)$  and its derivative satisfy the conditions

$$\phi(0) = 0, \quad \phi(l) = 0, \quad \phi'(0) = \theta_n, \quad \phi'(l) = \theta_j. \quad (3)$$

Here, the length  $l$  represents  $l_1$  ( $l_2$ ) for  $j = n - 1$  ( $j = n + 1$ ) when  $n$  is even, and  $l_2$  ( $l_1$ ) for  $j = n + 1$  ( $j = n - 1$ ) when  $n$  is odd. Using Eq. (2), we can solve  $C_1, C_2, C_3, C_4$ , but we only need  $C_4$  in the sequel:

$$C_4(\theta_j) = \frac{1}{2\beta} \left[ \frac{B(\beta l)}{A(\beta l)} \theta_n - \frac{C(\beta l)}{A(\beta l)} \theta_j \right], \quad (4)$$

where

$$A(\beta l) = 1 - \cosh \beta l \cos \beta l, \quad (5)$$

$$B(\beta l) = \sinh \beta l \cos \beta l - \cosh \beta l \sin \beta l, \quad (6)$$

$$C(\beta l) = \sinh \beta l - \sin \beta l. \quad (7)$$

Thus, the deflection  $\phi$  is expressed with  $|\theta\rangle$ ; and the bending moment at the  $n$ -th joint is given as  $M_n^j = EI\phi''(0) = 2EI\beta^2 C_4(\theta_j)$ .

Finally, the rotational angles  $|\theta\rangle$  at the joints are solved, by the balance equation of the bending moments  $\sum_{j=n-1, n+1} M_n^j = 0$ , which is expressed as

$$\begin{aligned} & \left[ \frac{B(\beta l_1)}{A(\beta l_1)} + \frac{B(\beta l_2)}{A(\beta l_2)} \right] \theta_n \\ & - \frac{C(\beta l_{2(1)})}{A(\beta l_{2(1)})} \theta_{n-1} - \frac{C(\beta l_{1(2)})}{A(\beta l_{1(2)})} \theta_{n+1} = 0. \end{aligned} \quad (8)$$

When  $n$  is odd, the coefficients  $C$  and  $A$  before  $\theta_{n-1(n+1)}$  in Eq. (8) are both functions of  $\beta l_{2(1)}$ ; when  $n$  is even, they are functions of  $\beta l_{1(2)}$ . Under fixed end boundary conditions shown in Fig. 1(a),  $\theta_{0(2N+1)} = 0$  should be substituted into Eq. (8) for the first and  $(2N)$ -th joints. Eq. (8) can be rewritten into a matrix form

$$H^{\text{beam}}|\theta\rangle = 0, \quad (9)$$

where  $H^{\text{beam}}$  is the dynamic matrix. The main-diagonal elements of  $H^{\text{beam}}$  are  $\left[ \frac{B(\beta l_1)}{A(\beta l_1)} + \frac{B(\beta l_2)}{A(\beta l_2)} \right]$ , and the sub-diagonal elements of  $H^{\text{beam}}$  are staggered numbers of  $-\frac{C(\beta l_1)}{A(\beta l_1)}$  and  $-\frac{C(\beta l_2)}{A(\beta l_2)}$ .

The dynamic matrix  $H^{\text{beam}}$  is analogous to the Hamiltonian matrix of the Su–Schrieffer–Heeger chain [21, 22], and the rotational angles of joints are analogous to the wavefunctions at the sites. Thus, with nontrivial topological properties, the natural frequencies of a finite structure will extend beyond the frequency range of the bulk bands of a boundary-free structure, manifested as the emergence of topological states. We prove the existence of topological states in the following.

*Existence of topological states.*—First, since the dynamic matrix of the continuous beam has chiral symmetry [22–25] (up to subtraction of a certain multiple of the identity matrix), the frequencies  $\beta_t$  of the topological edge states must correspond to the case that the main-diagonal elements of the dynamic matrix  $H^{\text{beam}}$  are 0, that is,

$$\frac{B(\beta_t l_1)}{A(\beta_t l_1)} + \frac{B(\beta_t l_2)}{A(\beta_t l_2)} = 0. \quad (10)$$

From Eq. (10), we solve the frequencies  $\beta_t$  where the topological states may occur. We observe that the function on the left-hand side of Eq. (10) is discontinuous when  $A(\beta l_1)A(\beta l_2) = 0$ , whose  $n$ -th positive root is denoted as  $\beta_0^{(n)}$  ( $n \geq 1$ ). It is noted that  $\beta_0^{(0)} = 0$  is also a root. Then, we prove the following Theorem (the proof is given in Supplemental Material Sec. A [26]):

**Theorem 1** *The frequencies of the topological edge states of a simply supported continuous beam with alternating spans  $l_1$  and  $l_2$  belong to the set  $\{\beta_t\}$  of all the positive roots of  $\frac{B(\beta l_1)}{A(\beta l_1)} + \frac{B(\beta l_2)}{A(\beta l_2)} = 0$ , where  $A(\beta l) = 1 - \cosh \beta l \cos \beta l$ ,  $B(\beta l) = \sinh \beta l \cos \beta l - \cosh \beta l \sin \beta l$ . There is one  $\beta_t$  in each interval  $(\beta_0^{(n-1)}, \beta_0^{(n)})$  of the roots of  $A(\beta l_1)A(\beta l_2) = 0$ .*

Second, for the set  $\{\beta_t\}$  containing all the frequencies of the topological edge states, we divide it into two subsets  $\{\beta_{t<}\}$  and  $\{\beta_{t>}\}$ , where  $\{\beta_t\} = \{\beta_{t<}\} \cup \{\beta_{t>}\}$ .  $\{\beta_{t<}\}$  is defined as the subset which contains  $\beta_{t<}^{(n)}$  satisfying

$$\left| \frac{C(\beta_t l_1)}{A(\beta_t l_1)} \right| < \left| \frac{C(\beta_t l_2)}{A(\beta_t l_2)} \right|, \quad (11)$$

and  $\{\beta_{t>}\}$  is defined as the subset which contains  $\beta_{t>}^{(n)}$  satisfying

$$\left| \frac{C(\beta_t l_1)}{A(\beta_t l_1)} \right| > \left| \frac{C(\beta_t l_2)}{A(\beta_t l_2)} \right|. \quad (12)$$

The topological states exist at  $\beta_{t<}^{(n)}$  in set  $\{\beta_{t<}\}$ , where the rotational angles at the joints and the deflections of the beam segments reach the maxima at the edges (for details see Supplemental Material Sec. B [26]); there are no topological states at frequencies in set  $\{\beta_{t>}\}$ . The case when  $\beta_t$  satisfies  $\left| \frac{C(\beta_t l_1)}{A(\beta_t l_1)} \right| = \left| \frac{C(\beta_t l_2)}{A(\beta_t l_2)} \right|$  corresponds to the topological phase transition point.

Then, we illustrate the frequency spectrum of a continuous beam with parameters  $l_1 = 40$  mm,  $l_2 = 50$  mm, and  $N = 16$  in Fig. 1(b). Degenerate topological edge states exist in certain intervals such as  $(\beta_0^{(0)}, \beta_0^{(1)})$ ,  $(\beta_0^{(2)}, \beta_0^{(3)})$ ,  $(\beta_0^{(4)}, \beta_0^{(5)})$ , and the frequencies of the topological states are  $\beta_t^{(1)}$ ,  $\beta_t^{(3)}$ ,  $\beta_t^{(5)}$ , etc., due to Eq. (11) (as illustrated in Supplemental Material Sec. A [26]). When the parameters are exchanged and taken as  $l_1 = 50$  mm,  $l_2 = 40$  mm, as shown in Fig. 1(c), topological edge states occur in the intervals where topological states are not seen in Fig. 1(b).

Third, under Bloch periodic boundary conditions, the dispersion relation of the continuous beam is given in Fig. 1(d). The dispersion relation for wave bands is detailed in Supplemental Material Sec. C [26]. By comparing the frequencies of the bulk bands and topological states in Fig. 1(b)–(d), when no band crossings occur (i.e.,  $\left| \frac{C(\beta_t l_1)}{A(\beta_t l_1)} \right| \neq \left| \frac{C(\beta_t l_2)}{A(\beta_t l_2)} \right|$ ), we have the following theorem (proof is given in Supplemental Material Sec. C [26]):

**Theorem 2** *There is one frequency band between two consecutive frequencies  $(\beta_t^{(n-1)}, \beta_t^{(n)})$  of the set  $\{\beta_t\}$ .*

Therefore, the bulk band between  $(\beta_t^{(n-1)}, \beta_t^{(n)})$  is the  $n$ -th frequency band, where  $\beta_t^{(0)} \equiv 0$ ; the bandgap between the  $n$ -th and  $(n+1)$ -th frequency bands is the  $n$ -th bandgap. Theorem 2 implies that all the topological states exist within the bandgaps.

We demonstrate the vibration modes of the localized topological edge states shown in Fig. 1(b) and (c). The topological edge modes ( $\beta = \beta_t^{(1)}$ ) in the first bandgap are shown on the top of Fig. 2(a), where each segment of the beam between two adjacent simple supports vibrates predominantly at its first-order mode. Due to the finite number of unit cells, there are two almost degenerate topological states at  $\beta = \beta_t^{(1)}$  (represented by  $\beta = \beta_t^{(1-1)}$  and  $\beta_t^{(1-2)}$ ), and the rotational angles are symmetrically and antisymmetrically distributed, which are localized at the leftmost and rightmost joints, so are the deflections. The topological edge modes in the third and fifth bandgaps ( $\beta = \beta_t^{(3)}$  and  $\beta = \beta_t^{(5)}$ ) are also shown in

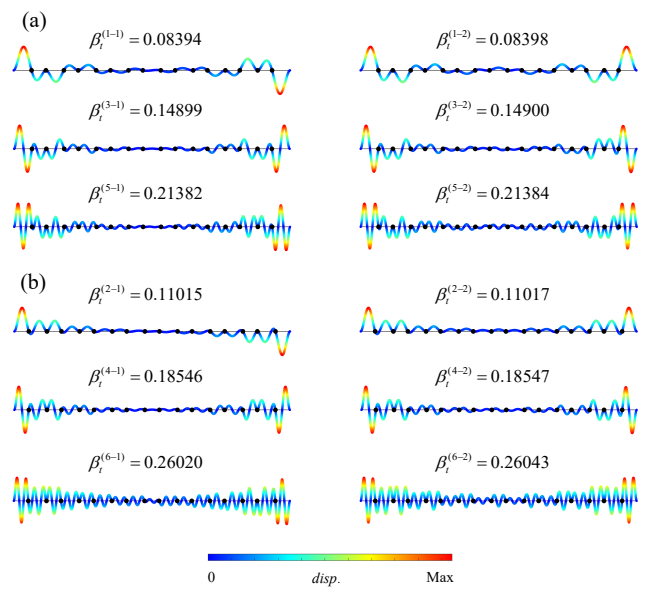


FIG. 2. Topological modes at the first-, second- and third-order modes of the continuous beam with  $l_1 = 40$  mm and  $l_2 = 50$  mm (a),  $l_1 = 50$  mm and  $l_2 = 40$  mm (b).

Fig. 2(a), where each segment is at its second- and third-order mode shapes, respectively. Similarly, the topological edge states in the second, fourth, and sixth bandgaps ( $\beta = \beta_t^{(2)}$ ,  $\beta_t^{(4)}$ ,  $\beta_t^{(6)}$ ) are shown in Fig. 2(b), where the segments vibrate at their first-, second-, and third-order modes. These theoretical results are verified by numerical simulations in Supplemental Material Sec. D [26].

Finally, we introduce a *topological index*  $\mu^{(n)}$  related to the bulk Zak phase [27–29] to determine the topological edge states, which is defined as

$$\mu^{(n)} = \gamma^{(n)} + \pi \cdot l^{(n)} \quad \text{mod } 2\pi, \quad (13)$$

where the Zak phase  $\gamma^{(n)}$  for the  $n$ -th bulk band is

$$\gamma^{(n)} = i \int_{-\pi/L}^{\pi/L} dk \langle \theta^{(n)} | \partial_k | \theta^{(n)} \rangle \quad \text{mod } 2\pi, \quad (14)$$

and  $l^{(n)}$  denotes the number of “eigenvalue crossing” occurring at positive eigenvalues within the frequency range  $(\beta_t^{(n-1)}, \beta_t^{(n)})$  of the  $n$ -th bulk band. When  $\mu^{(n)} = \pi$ , nontrivial topological edge states must exist in the  $n$ -th bandgap; when  $\mu^{(n)} = 0$ , there are no topological edge states. The criterion Eq. (13) *strictly establishes the bulk–edge correspondence* [22, 30] and gives the same results as predicted via Eqs. (11) and (12). For details and derivations, see Supplemental Material Sec. E [26].

*Topological dynamics of lattice structures.*—The theoretical framework we built above for continuous beams is powerful in that it is directly applicable to general planar continuum lattice structures such as bridge-like frames [Fig. 3(a)], kagome frames [Fig. 3(b)], and even homogeneous plates [Fig. 3(c)] (for detailed methods see

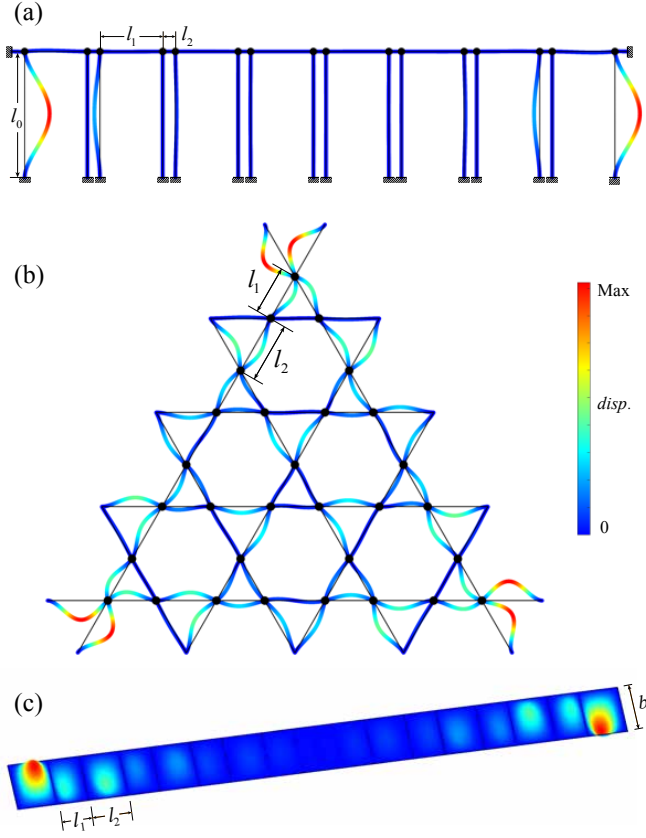


FIG. 3. (a) A topological edge state of a bridge-like frame structure with lengths of horizontal beams  $l_1 = 50$  mm,  $l_2 = 10$  mm, and vertical beams  $l_0 = 100$  mm. The thin black lines indicate the positions of the frames before deformation. (b) A topological corner state in a kagome frame structure with  $l_1 = 40$  mm,  $l_2 = 50$  mm. (c) A topological edge state in a plate with lengths  $l_1 = 40$  mm,  $l_2 = 50$  mm and width  $b = 100$  mm.

Supplemental Material Sec. F [26]). For a bridge-like frame structure, the lengths of the horizontal and vertical beams are taken as  $l_{1,2}$  and  $l_0$ , respectively. All boundary conditions for the outermost ends are clamped. The bulk bands are separated from the topological edge states when  $\left| \frac{C(\beta_t l_1)}{A(\beta_t l_1)} \right| \neq \left| \frac{C(\beta_t l_2)}{A(\beta_t l_2)} \right|$ ; and there are topological states in the first bandgap [Fig. 3(a)] when  $l_1 > l_2$  ( $l_{1,2}$  are supposed to be distinctly separated from  $l_0$ ). A kagome frame structure with  $C_3$  symmetry [31, 32], as shown in Fig. 3(b), is constructed with alternately arranged beams with lengths  $l_1$  and  $l_2$ . Since the kagome lattice has generalized chiral symmetry [33], the topological corner states correspond to the frequencies  $\beta_t$  where main diagonal elements  $2 \sum_{i=1}^2 \frac{B(\beta l_i)}{A(\beta l_i)}$  are all 0, as shown in Fig. 3(b). For a homogeneous plate where the edges  $y = 0$  and  $y = b$  are simply supported, the edges  $x = 0$  and  $x = N \cdot (l_1 + l_2) + l_2$  are clamped, and simple supports are set to separate it into lengths  $l_2, l_1, l_2, \dots, l_1, l_2$  along the  $x$ -direction [Fig. 3(c)], it has decoupled

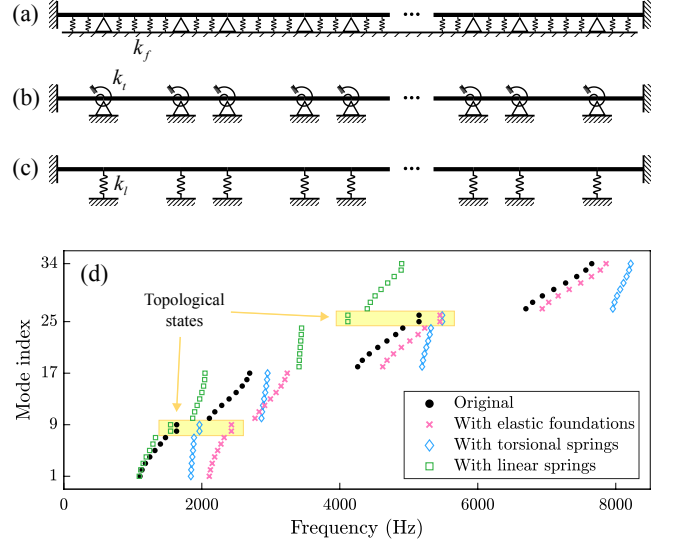


FIG. 4. (a)–(c) Continuous beams on the Winkler elastic foundation, torsional springs, and linear springs. (d) The frequency spectra of the three structures. The eigenfrequencies of the topological states are shifted from those of the original structure when springs are added ( $k_f = 375EI/l_1^4$ ,  $k_t = 30EI/l_1$ , and  $k_l = 750EI/l_1^3$ ).

deflections in two orthogonal directions, with nontrivial topological properties along the  $x$ -direction. Each section of the plate perpendicular to the  $y$ -axis has a mode profile localized near the edges  $x = 0$  and  $x = N \cdot (l_1 + l_2) + l_2$ .

The theoretical method is also extended to variants of continuous beam structures by introducing elastic springs, so that we can achieve precise *modulations* of the frequencies of the topological states. If a continuous beam is supported on *Winkler elastic foundations* with spring constant  $k_f$  as shown in Fig. 4(a), the relation between the eigenfrequencies of the beam structures with and without elastic foundations is  $\omega_f^2 = \omega^2 + k_f/m$ . If *torsional springs*  $k_t$  are present at the joints as shown in Fig. 4(b),  $\beta_t^{(n)}$  of the topological states becomes larger compared to the original  $\beta$ ; however, it does not exceed the upper bound  $\beta_0^{(n)}$  of the interval  $(\beta_0^{(n-1)}, \beta_0^{(n)})$ . If a continuous beam is supported on discrete *linear springs*  $k_l$ , as shown in Fig. 4(c), the linear springs are regarded as a disturbance to the original structure (analogous to the effect of next-nearest-neighbor hoppings for extended SSH chains). In this case, the degree of localization of the topological states decreases with the decrease of  $k_l$ . The frequency spectra containing the topological states with the first two modes of the three types of supported beams are shown in Fig. 4(d).

*Conclusion.*—In this Letter, we rigorously identify the infinitely many topological edge states of continuous beam structures, by introducing a topological index related to the Zak phases. We directly apply the theoretical approach to reveal the topological dynamics of several

typical continuum lattice structures including continuous beams supported on elastic foundations, torsional springs, and linear springs, as well as bridge-like frame structures, kagome frame structures, and homogeneous plates, which verifies the universality and applicability of our theory. The continuum lattice structures serve as excellent platforms for exploring various kinds of topological phases and demonstrating the topologically protected states at multifrequencies, due to their simple configurations and the concise theoretical framework. Lattice structures extensively exist in buildings, bridges, railways, ships, advanced microstructural materials etc., and thus the topological dynamics of continuum lattice structures has significant implications in safety assessment, structural health monitoring, and energy harvesting.

Y. S., J. X. and J. W. thank the National Natural Science Foundation of China (Grants No. 11991033), and L.-H. S. thanks the Beijing Natural Science Foundation (Grant No. JQ21001), for support of this work.

---

\* Corresponding author.

jxwang@pku.edu.cn

- [1] J. Solon, A. Kaya-Çopur, J. Colombelli, and D. Brunner, Pulsed forces timed by a ratchet-like mechanism drive directed tissue movement during dorsal closure, *Cell* **137**, 1331 (2009).
- [2] S.-Z. Lin, B. Li, G. Lan, and X.-Q. Feng, Activation and synchronization of the oscillatory morphodynamics in multicellular monolayer, *Proc. Natl. Acad. Sci.* **114**, 8157 (2017).
- [3] Y. Jiang, D. Yan, J. Wang, L.-H. Shao, and P. Sharma, The giant flexoelectric effect in a luffa plant-based sponge for green devices and energy harvesters, *Proc. Natl. Acad. Sci.* **120**, e2311755120 (2023).
- [4] M. C. Fernandes, J. Aizenberg, J. C. Weaver, and K. Bertoldi, Mechanically robust lattices inspired by deep-sea glass sponges, *Nat. Mater.* **20**, 237 (2021).
- [5] T. A. Schaedler, A. J. Jacobsen, A. Torrents, A. E. Sorensen, J. Lian, J. R. Greer, L. Valdevit, and W. B. Carter, Ultralight metallic microlattices, *Science* **334**, 962 (2011).
- [6] M. Ashby, The properties of foams and lattices, *Phil. Trans. R. Soc. A* **364**, 15 (2006).
- [7] D. Yan, J. Wang, J. Xiang, Y. Xing, and L.-H. Shao, A flexoelectricity-enabled ultrahigh piezoelectric effect of a polymeric composite foam as a strain-gradient electric generator, *Sci. Adv.* **9**, eadc8845 (2023).
- [8] H. Liu, Q. Zhang, K. Zhang, G. Hu, and H. Duan, Designing 3d digital metamaterial for elastic waves: From elastic wave polarizer to vibration control, *Adv. Sci.* **6**, 1900401 (2019).
- [9] A. S. Phani, J. Woodhouse, and N. A. Fleck, Wave propagation in two-dimensional periodic lattices, *J. Acoust. Soc. Am.* **119**, 1995 (2006).
- [10] G. C. Thiang and H. Zhang, Bulk-interface correspondences for one-dimensional topological materials with inversion symmetry, *Proc. R. Soc. A* **479**, 20220675 (2023).
- [11] H. Chen, H. Nassar, and G. Huang, A study of topological effects in 1D and 2D mechanical lattices, *J. Mech. Phys. Solids* **117**, 22 (2018).
- [12] Y. Chen, X. Liu, and G. Hu, Topological phase transition in mechanical honeycomb lattice, *J. Mech. Phys. Solids* **122**, 54 (2019).
- [13] D. Zhao, M. Xiao, C. W. Ling, C. T. Chan, and K. H. Fung, Topological interface modes in local resonant acoustic systems, *Phys. Rev. B* **98**, 014110 (2018).
- [14] X. Shi, I. Kiropelidis, R. Chaunsali, V. Achilleos, G. Theocharis, and J. Yang, Disorder-induced topological phase transition in a one-dimensional mechanical system, *Phys. Rev. Res.* **3**, 033012 (2021).
- [15] M. I. N. Rosa, R. K. Pal, J. R. F. Arruda, and M. Ruzzene, Edge states and topological pumping in spatially modulated elastic lattices, *Phys. Rev. Lett.* **123**, 034301 (2019).
- [16] H. Fan, B. Xia, L. Tong, S. Zheng, and D. Yu, Elastic higher-order topological insulator with topologically protected corner states, *Phys. Rev. Lett.* **122**, 204301 (2019).
- [17] Z. Zheng, J. Yin, J. Wen, and D. Yu, Multiple topological interface states in broadband locally resonant phononic crystals, *J. Appl. Phys.* **129**, 184901 (2021).
- [18] J. Yin, M. Ruzzene, J. Wen, D. Yu, L. Cai, and L. Yue, Band transition and topological interface modes in 1D elastic phononic crystals, *Sci. Rep.* **8**, 6806 (2018).
- [19] Muhammad, W. Zhou, and C. Lim, Topological edge modeling and localization of protected interface modes in 1d phononic crystals for longitudinal and bending elastic waves, *Int. J. Mech. Sci.* **159**, 359 (2019).
- [20] S. S. Rao, *Vibration of continuous systems* (Wiley, Hoboken, NJ, 2019) Chap. 11, 2nd ed.
- [21] W. P. Su, J. R. Schrieffer, and A. J. Heeger, Solitons in polyacetylene, *Phys. Rev. Lett.* **42**, 1698 (1979).
- [22] J. K. Asbóth, L. Oroszlány, and A. Pályi, *A Short Course on Topological Insulators* (Springer, Cham, 2016).
- [23] A. P. Schnyder, S. Ryu, A. Furusaki, and A. W. W. Ludwig, Classification of topological insulators and superconductors in three spatial dimensions, *Phys. Rev. B* **78**, 195125 (2008).
- [24] C.-K. Chiu, J. C. Y. Teo, A. P. Schnyder, and S. Ryu, Classification of topological quantum matter with symmetries, *Rev. Mod. Phys.* **88**, 035005 (2016).
- [25] M. Maffei, A. Dauphin, F. Cardano, M. Lewenstein, and P. Massignan, Topological characterization of chiral models through their long time dynamics, *New J. Phys.* **20**, 013023 (2018).
- [26] See Supplemental Material for (A) proof of the existence of topological states, (B) localization characteristics of topological states, (C) proof of the existence of frequency bands and topological states within bandgaps, (D) numerical results of topological edge states of continuous beam structures, (E) relation of the topological index and Zak phase for continuous beam structure, (F) theoretical framework for general continuum lattice structure, which includes Refs. [34, 35].
- [27] J. Zak, Berry's phase for energy bands in solids, *Phys. Rev. Lett.* **62**, 2747 (1989).
- [28] M. Xiao, G. Ma, Z. Yang, P. Sheng, Z. Q. Zhang, and C. T. Chan, Geometric phase and band inversion in periodic acoustic systems, *Nat. Phys.* **11**, 240 (2015).
- [29] G. van Miert, C. Ortix, and C. M. Smith, Topological origin of edge states in two-dimensional inversion-symmetric insulators and semimetals, *2D Mater.* **4**, 015023 (2017).
- [30] M. Xiao, Z. Q. Zhang, and C. T. Chan, Surface

- impedance and bulk band geometric phases in one-dimensional systems, *Phys. Rev. X* **4**, 021017 (2014).
- [31] W. A. Benalcazar, T. Li, and T. L. Hughes, Quantization of fractional corner charge in  $C_n$ -symmetric higher-order topological crystalline insulators, *Phys. Rev. B* **99**, 245151 (2019).
- [32] C. W. Peterson, T. Li, W. A. Benalcazar, T. L. Hughes, and G. Bahl, A fractional corner anomaly reveals higher-order topology, *Science* **368**, 1114 (2020).
- [33] X. Ni, M. Weiner, A. Alù, and A. B. Khanikaev, Observation of higher-order topological acoustic states protected by generalized chiral symmetry, *Nat. Mater.* **18**, 113 (2019).
- [34] T. L. Hughes, E. Prodan, and B. A. Bernevig, Inversion-symmetric topological insulators, *Phys. Rev. B* **83**, 245132 (2011).
- [35] J. Lin and H. Zhang, Mathematical theory for topological photonic materials in one dimension, *J. Phys. A: Math. Theor.* **55**, 495203 (2022).

# Supplemental Material for Topological dynamics of continuum lattice structures

Yimeng Sun,<sup>1</sup> Jiacheng Xing,<sup>1</sup> Li-Hua Shao,<sup>2</sup> and Jianxiang Wang<sup>1,\*</sup>

<sup>1</sup>*Department of Mechanics and Engineering Science,*

*College of Engineering, Peking University, Beijing 100871, China*

<sup>2</sup>*School of Aeronautic Science and Engineering, Beihang University, Beijing 100191, China*

## A: Proof of the existence of topological states

In this section, we prove Theorem 1 in the main text. If we want to prove the existence of topological states, first of all, we must prove the existence of the solutions to Eq. (10). We examine the properties of the function  $\frac{B(\beta l)}{A(\beta l)}$  when  $l$  is fixed: note that the function  $\frac{B(\beta l)}{A(\beta l)}$  is continuously differentiable with respect to  $\beta$  when the denominator  $A(\beta l) \neq 0$ , so we have

$$\frac{1}{l} \frac{d}{d\beta} \left[ \frac{B(\beta l)}{A(\beta l)} \right] = \frac{B' \cdot A - B \cdot A'}{A^2} = \frac{(\sinh \beta l - \sin \beta l)^2}{A^2} = \frac{C^2}{A^2} > 0, \quad (\text{A1})$$

where  $A' = -B$  (the prime denotes differentiation with respect to the argument  $\beta l$ ), indicating that the function  $\frac{B(\beta l)}{A(\beta l)}$  increases monotonically with  $\beta$  in any interval in which  $A(\beta l) \neq 0$ . Since the roots  $\beta_0$  of  $A(\beta l) = 1 - \cosh \beta l \cos \beta l = 0$  satisfy  $\beta_0 l > 3\pi/2$ , we have  $\frac{1}{\cos \beta_0 l} = \cosh \beta_0 l > \sqrt{2}$ , i.e.,  $|\tan \beta_0 l| > 1$ . And since  $-1 < \tanh \beta_0 l < 1$ , we have

$$B(\beta_0 l) = \cos \beta_0 l \sinh \beta_0 l - \sin \beta_0 l \cosh \beta_0 l = \tanh \beta_0 l - \tan \beta_0 l \neq 0,$$

that is, the zeros of function  $A(\beta l)$  do not coincide with the zeros of  $B(\beta l)$ . Therefore, when  $A(\beta_0 l) = 0$ , the values of  $B(\beta_0 l)$  are finite, and hence  $\frac{B(\beta_0 l)}{A(\beta_0 l)} \rightarrow \infty$ .

Next, we examine the properties of  $\left[ \frac{B(\beta l_1)}{A(\beta l_1)} + \frac{B(\beta l_2)}{A(\beta l_2)} \right]$  as a function of  $\beta$ . The  $\beta_0$ 's which render the denominators  $A(\beta_0 l_1) = 0$  and  $A(\beta_0 l_2) = 0$  divide the frequencies  $\beta$  into multiple intervals; and at each root  $\beta_0$ ,  $\left[ \frac{B(\beta_0 l_1)}{A(\beta_0 l_1)} + \frac{B(\beta_0 l_2)}{A(\beta_0 l_2)} \right] \rightarrow \infty$ . From Eq. (A1), we know that the function  $\left[ \frac{B(\beta l_1)}{A(\beta l_1)} + \frac{B(\beta l_2)}{A(\beta l_2)} \right]$  increases monotonically in each interval  $(\beta_0^{(n-1)}, \beta_0^{(n)})$ . That is, in each interval, the function  $\left[ \frac{B(\beta l_1)}{A(\beta l_1)} + \frac{B(\beta l_2)}{A(\beta l_2)} \right]$  increases monotonically from  $-\infty$  to  $+\infty$ ; thus it has one and only one root  $\beta_t^{(n)}$  in each interval  $(\beta_0^{(n-1)}, \beta_0^{(n)})$ . Theorem 1 is proved.

Finally, we give an example to better illustrate the above proof. The structure under the cyclic boundary condition (i.e., Born-von Karman boundary condition) is considered, where we take  $\theta_0 = \theta_{2N}$  and  $\theta_{2N+1} = \theta_1$  in the balance equations of the first and  $(2N)$ -th joints. Similarly, Eq. (8) can be rewritten into a matrix equation  $H_{\text{B-K}}^{\text{beam}}|\theta\rangle = 0$ , whose solutions  $\beta$  correspond to the frequency bands of a boundary-free continuous beam structure. Under the Born-von Karman boundary condition, with parameters  $l_1 = 40$  mm,  $l_2 = 50$  mm, and  $N = 16$ , Fig. S1(a) depicts all the eigenvalues  $y$  (ordinate) of the matrix  $H_{\text{B-K}}^{\text{beam}}$  as  $\beta$  (abscissa) varies continuously. The natural frequencies  $\beta$  of the periodic continuous beam structure (i.e., the solutions of  $H_{\text{B-K}}^{\text{beam}}|\theta\rangle = 0$ ) are manifested in Fig. S1(a) as all intersection points of the black curves and the gray straight line  $y = 0$ , which are piecewise distributed across the spectrum. The pink vertical lines in Fig. S1(a) represent the roots of the equation  $A(\beta_0 l_2) = 0$ , and the green vertical lines represent the roots of  $A(\beta_0 l_1) = 0$ ; all vertical lines correspond to  $\beta = \beta_0^{(n)}$ . There is only one blue dashed curve between every

\* Corresponding author.  
jxwang@pku.edu.cn

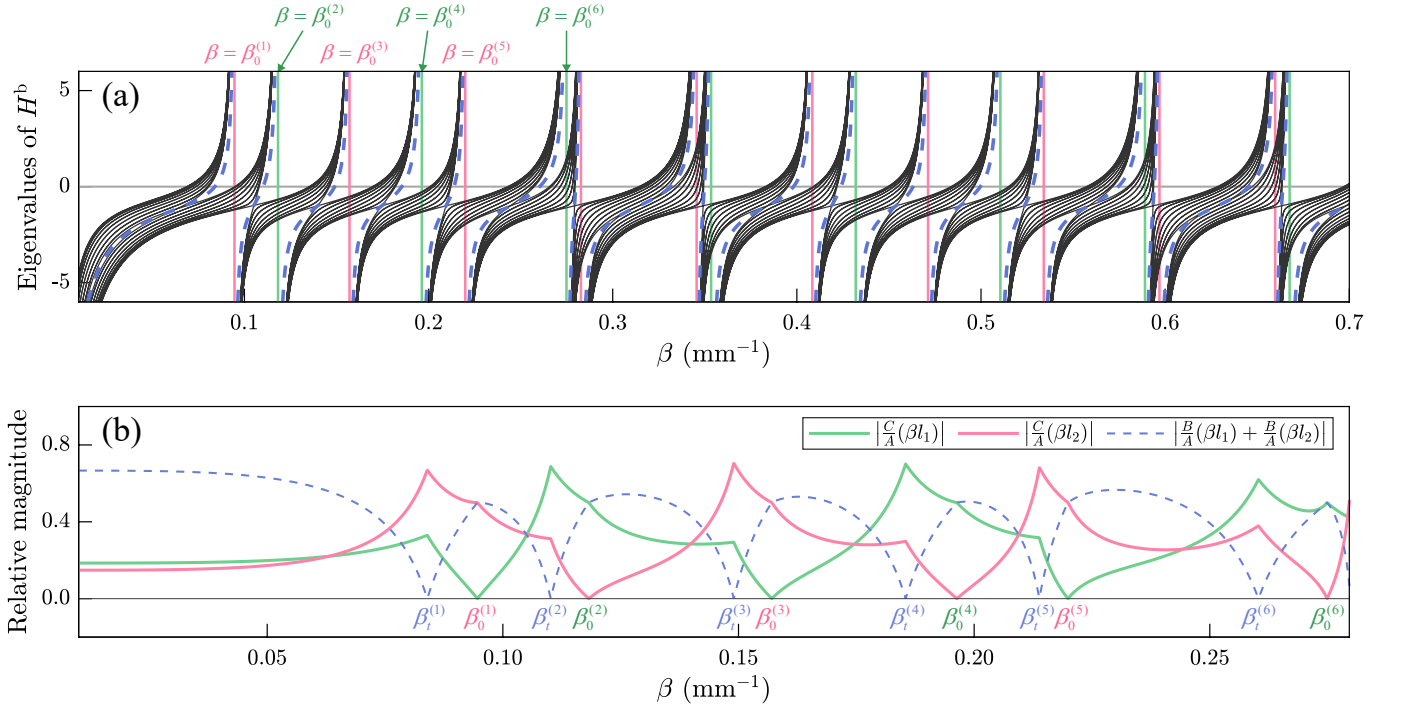


FIG. S1. (a) Bulk bands of the boundary-free continuous beam structure (corresponding to all intersections of the black curves with the horizontal gray straight line) and frequencies at which topological states may exist (the intersections of the blue dashed curves with the horizontal gray straight line). The pink (green) vertical lines represent the roots of the equation  $A(\beta_0 l_{2(1)}) = 0$ . (b) Relative magnitudes of subdiagonal elements  $\frac{C}{A}(\beta l_1)$  and  $\frac{C}{A}(\beta l_2)$  for the continuous beam structure with  $l_1 = 40$  mm and  $l_2 = 50$  mm. The frequency  $\beta_t^{(n)}$  in each interval  $(\beta_0^{(n-1)}, \beta_0^{(n)})$  belongs to the set  $\{\beta_t\}$  containing the frequencies of topological states; an edge state exists if and only if  $|\frac{C}{A}(\beta_t l_1)| < |\frac{C}{A}(\beta_t l_2)|$  at  $\beta_t^{(n)}$ . The plotted functions are normalized, and only their relative heights are meaningful.

two vertical lines, which represents the value of function  $[\frac{B(\beta l_1)}{A(\beta l_1)} + \frac{B(\beta l_2)}{A(\beta l_2)}]$ ; it can be seen that the blue curve increases monotonically from  $-\infty$  to  $+\infty$  within each interval  $(\beta_0^{(n-1)}, \beta_0^{(n)})$ , and the intersections of the blue curve with  $y = 0$  correspond to the solution of Eq. (10) (i.e.,  $\beta_t^{(n)}$ ). Thus we can see from Fig. S1(a) that there exists one and only one frequency  $\beta_t^{(n)}$  (which belongs to the set  $\{\beta_t\}$  containing the frequencies of topological edge states) within each interval  $(\beta_0^{(n-1)}, \beta_0^{(n)})$  for the continuous beam structure.

Then, we illustrate that topological states exist and only exist at frequency  $\beta_t^{(n)}$  when  $|\frac{C(\beta_t l_1)}{A(\beta_t l_1)}| < |\frac{C(\beta_t l_2)}{A(\beta_t l_2)}|$ , with an exemplified continuous beam structure with parameters  $l_1 = 40$  mm,  $l_2 = 50$  mm. As shown in Fig. S1(b),  $|\frac{C(\beta_t l_1)}{A(\beta_t l_1)}| < |\frac{C(\beta_t l_2)}{A(\beta_t l_2)}|$  is established at  $\beta_t^{(1)}$ ,  $\beta_t^{(3)}$ , and  $\beta_t^{(5)}$ ; thus we find degenerate topological states at these frequencies as shown in Fig. 1(b).

## B: Localization characteristics of topological states

In this section, we illustrate the localization characteristics of the topological state at the left boundary, while the right boundary is similar. Because  $H^{\text{beam}}(\beta_t)$  in Eq. (9) has chiral symmetry  $\Gamma H^{\text{beam}}(\beta_t) = -H^{\text{beam}}(\beta_t)\Gamma$ , where  $\Gamma = I_N \otimes \sigma_z$  ( $\sigma_z$  is the Pauli matrix), thus  $H^{\text{beam}}(\beta_t)\Gamma_B|\theta\rangle = 0$  [where  $\Gamma_B = (I - \Gamma)/2$  is the projection matrix onto even-numbered joints], implying that the rotational angles at the even-numbered joints of the topological state at the left boundary are zero. For the odd-numbered joints, from Eq. (9), we know that the rotational angles reach the maximum value at the first node and decay exponentially away from the left edge with  $\theta_{n+2} = c_{\text{decay}} \cdot \theta_n$ , where



$c_{\text{decay}} = -[C(\beta_t l_1)A(\beta_t l_2)]/[C(\beta_t l_2)A(\beta_t l_1)]$  and  $|c_{\text{decay}}| < 1$ .

The localization is also manifested in the deflections of beam segments as shown in Fig. 2(a),(b). We show the localization at the left boundary in the beams with length  $l_1$  as an example. The joint rotational angles  $\theta_3$  and  $\theta_4$  are just a rescaling of the angles  $\theta_1$  and  $\theta_2$  (note that  $\theta_{2n}$  is essentially zero near the left boundary due to the chiral symmetry). Because Eq. (3) is linear with respect to  $C_{1,2,3,4}$  and  $\theta_{n,j}$ , the deflection of the fourth beam is also a simple rescaling of the deflection of the second beam, with the same scaling coefficient  $c_{\text{decay}}$  as that of the angles,  $\theta_3/\theta_1$ . For all beams with length  $l_1$ , the beam deflections reach the maximum value at the beam between the first and second joints and decay exponentially away from the left edge; the case for beams with length  $l_2$  is similar.

### C: Proof of the existence of frequency bands and topological states within bandgaps

In this section, we prove Theorem 2 in the main text. We first determine the locations of the bulk bands by an infinite Bloch-periodic continuous beam structure. For an infinite continuous beam structure, the periodic unit cell is shown in Fig. 1(a), and the rotational angles of the joints at sublattices A and B in the  $m$ -th unit cell are  $\theta_A^m$  and  $\theta_B^m$ . The dynamic equations are

$$\left[ \frac{B(\beta l_1)}{A(\beta l_1)} + \frac{B(\beta l_2)}{A(\beta l_2)} \right] \theta_A^m - \frac{C(\beta l_2)}{A(\beta l_2)} \theta_B^{m-1} - \frac{C(\beta l_1)}{A(\beta l_1)} \theta_B^m = 0, \quad (\text{C1})$$

$$\left[ \frac{B(\beta l_1)}{A(\beta l_1)} + \frac{B(\beta l_2)}{A(\beta l_2)} \right] \theta_B^m - \frac{C(\beta l_1)}{A(\beta l_1)} \theta_A^m - \frac{C(\beta l_2)}{A(\beta l_2)} \theta_A^{m+1} = 0. \quad (\text{C2})$$

Substituting Bloch's theorem  $\theta_{A(B)}^{m+1} = e^{ikL} \theta_{A(B)}^m$  into Eqs. (C1) and (C2), we obtain

$$H_{\text{Bloch}}^{\text{beam}}|\theta\rangle = \begin{bmatrix} \frac{B(\beta l_1)}{A(\beta l_1)} + \frac{B(\beta l_2)}{A(\beta l_2)} & -\frac{C(\beta l_1)}{A(\beta l_1)} - \frac{C(\beta l_2)}{A(\beta l_2)} \cdot e^{-ikL} \\ -\frac{C(\beta l_1)}{A(\beta l_1)} - \frac{C(\beta l_2)}{A(\beta l_2)} \cdot e^{ikL} & \frac{B(\beta l_1)}{A(\beta l_1)} + \frac{B(\beta l_2)}{A(\beta l_2)} \end{bmatrix} \begin{bmatrix} \theta_A^m \\ \theta_B^m \end{bmatrix} = 0, \quad (\text{C3})$$

where  $L = l_1 + l_2$  is the lattice constant. For Eq. (C3) to have nontrivial solutions, it must hold that

$$\frac{B(\beta l_1)}{A(\beta l_1)} + \frac{B(\beta l_2)}{A(\beta l_2)} = \pm \sqrt{\left[ \frac{C(\beta l_1)}{A(\beta l_1)} \right]^2 + \left[ \frac{C(\beta l_2)}{A(\beta l_2)} \right]^2 + 2 \frac{C(\beta l_1) C(\beta l_2)}{A(\beta l_1) A(\beta l_2)} \cos kL}. \quad (\text{C4})$$

Solutions of Eq. (C4) correspond to the range of the frequency bands, which are symmetric under an exchange of  $l_1$  and  $l_2$ . The dispersion relation solved from Eq. (C4) is shown in Fig. 1(d). To prove that the topological states do not overlap with the range of bulk bands, Eq. (C4) is rewritten into

$$\left[ \frac{B(\beta l_1)}{A(\beta l_1)} + \frac{B(\beta l_2)}{A(\beta l_2)} \right]^2 = \left[ \frac{C(\beta l_1)}{A(\beta l_1)} + \frac{C(\beta l_2)}{A(\beta l_2)} \right]^2 + \frac{2C(\beta l_1)C(\beta l_2)}{A(\beta l_1)A(\beta l_2)} (\cos kL - 1), \quad (\text{C5})$$

$$\left[ \frac{B(\beta l_1)}{A(\beta l_1)} + \frac{B(\beta l_2)}{A(\beta l_2)} \right]^2 = \left[ \frac{C(\beta l_1)}{A(\beta l_1)} - \frac{C(\beta l_2)}{A(\beta l_2)} \right]^2 + \frac{2C(\beta l_1)C(\beta l_2)}{A(\beta l_1)A(\beta l_2)} (\cos kL + 1). \quad (\text{C6})$$

Since  $\frac{B}{A}(\beta_t l_1) + \frac{B}{A}(\beta_t l_2) = 0$  holds at frequencies of the topological states, we substitute it into Eqs. (C5) and (C6), rendering the left-hand sides both equal to 0. When  $|\frac{C}{A}(\beta_t l_1)| \neq |\frac{C}{A}(\beta_t l_2)|$ , if  $\frac{C(\beta l_1)C(\beta l_2)}{A(\beta l_1)A(\beta l_2)} \leq 0$ , the right-hand side of Eq. (C5) is larger than 0; if  $\frac{C(\beta l_1)C(\beta l_2)}{A(\beta l_1)A(\beta l_2)} > 0$ , the right-hand side of Eq. (C6) becomes larger than 0. In conclusion, under the condition of  $|\frac{C}{A}(\beta_t l_1)| \neq |\frac{C}{A}(\beta_t l_2)|$ , the frequencies corresponding to the topological states are not within the solution range of the periodic frequency bands [that is, frequencies  $\beta = \beta_t$  are not the solutions of Eq. (C4) for any value of  $kL$ ], so the topological states do not overlap with the frequency bands. We note that the exceptional points of  $|\frac{C}{A}(\beta_t l_1)| = |\frac{C}{A}(\beta_t l_2)|$  in rare cases correspond to the Dirac points where two bulk bands touch, closing the bandgap.

Next, we continue to prove that there must be a frequency band between every two consecutive frequencies  $(\beta_t^{(n-1)}, \beta_t^{(n)})$  of the set  $\{\beta_t\}$  containing the frequencies of topological states, that is, the solutions of Eq. (C4) exist in each interval  $(\beta_t^{(n-1)}, \beta_t^{(n)})$  for any  $k$  in the Brillouin zone. We define a function

$$f(\beta) \equiv \left[ \frac{C(\beta l_1)}{A(\beta l_1)} \right]^2 + \left[ \frac{C(\beta l_2)}{A(\beta l_2)} \right]^2 - \left[ \frac{B(\beta l_1)}{A(\beta l_1)} \right]^2 - \left[ \frac{B(\beta l_2)}{A(\beta l_2)} \right]^2 + \frac{2C(\beta l_1)C(\beta l_2)}{A(\beta l_1)A(\beta l_2)} \cos kL - \frac{2B(\beta l_1)B(\beta l_2)}{A(\beta l_1)A(\beta l_2)}. \quad (\text{C7})$$

From the analysis in the previous paragraph, we know that  $f(\beta_t) > 0$  and takes a finite value when  $|\frac{C}{A}(\beta_t l_1)| \neq |\frac{C}{A}(\beta_t l_2)|$ . Meanwhile, from Theorem 1 in Section A,  $\beta_0^{(n)}$  which satisfies  $A(\beta_0^{(n)} l_1) = 0$  or  $A(\beta_0^{(n)} l_2) = 0$  must exist in the interval  $(\beta_t^{(n-1)}, \beta_t^{(n)})$ . Since

$$C^2(\beta l) - B^2(\beta l) = -2 \sinh(\beta l) \sin(\beta l) \cdot A(\beta l), \quad (\text{C8})$$

considering the behavior of  $f(\beta)$  around  $\beta = \beta_0^{(n)}$  when  $A(\beta l_1) \rightarrow 0^\pm$  (the case  $A(\beta l_2) \rightarrow 0^\pm$  is analogous), we have

$$\begin{aligned} f(\beta) &= \left[ \frac{C(\beta l_1)}{A(\beta l_1)} \right]^2 - \left[ \frac{B(\beta l_1)}{A(\beta l_1)} \right]^2 + \left[ \frac{2C(\beta l_1)C(\beta l_2) \cos kL - 2B(\beta l_1)B(\beta l_2)}{A(\beta l_2)} \right] \frac{1}{A(\beta l_1)} + O(1) \\ &= \frac{1}{A(\beta l_1)} \left[ -2 \sinh(\beta l_1) \sin(\beta l_1) + \frac{2C(\beta l_1)C(\beta l_2) \cos kL - 2B(\beta l_1)B(\beta l_2)}{A(\beta l_2)} \right] + O(1), \end{aligned} \quad (\text{C9})$$

and thus  $f(\beta) \rightarrow \pm\infty$  ( $\beta \rightarrow \beta_0^{(n)\pm}$ ). In terms of this result and the condition that  $f(\beta_t) > 0$ , for each given  $kL \in (-\pi, \pi]$ , there must exist a zero point of  $f(\beta) = 0$  between the frequencies  $(\beta_t^{(n-1)}, \beta_t^{(n)})$ , that is, Eq. (C4) must have a solution between the interval  $(\beta_t^{(n-1)}, \beta_t^{(n)})$ , and hence there must be a frequency band between the adjacent frequencies of topological states. Through the above proofs, we find that the topological states exist within the bandgaps and do not overlap with the frequency bands. Theorem 2 is proved. The spectra obtained from example structures – Figs. 1(b),(c) in the main text – also show the existence of frequency bands between topological states and the phenomenon that the topological states and frequency bands do not overlap, verifying our theoretical proof.

#### D: Numerical results of topological edge states of continuous beam structures

In this section, we give the detailed numerical results of topological edge states, verifying the theoretical conclusions. We construct a continuous beam structure using the beam module in the structural mechanics branch of COMSOL Multiphysics. The material is structural steel, with elastic modulus  $200 \times 10^9$  Pa, density  $7850$  kg/m<sup>3</sup>, and Poisson's ratio 0.3. The cross-sections are all selected as rectangular sections with width and height of 1 mm. The total length of the continuous beam is consistent with the theoretical model where  $N = 8$ .

First, the length intervals of the simple supports in the continuous beam are set to  $l_1 = 40$  mm and  $l_2 = 50$  mm, and then the natural frequencies of the continuous beam structure are calculated. As shown in Fig. S2(a), the black solid dots represent the spectrum composed of 51 modes at the lowest frequencies of the structure. The first-order vibration modes of the continuous beam structure (whose beam segment between every two supports are at their first-order mode shapes) correspond to the 1st–17th modes, of which the 8th mode with a frequency of 1544.6 Hz and the 9th mode with a frequency of 1560.1 Hz correspond to the topological edge states, and the rotational angles of the topological states with first-order vibration modes are localized at the leftmost and rightmost joints of the continuous beam as shown in Fig. S2(b). The second-order vibration modes of the continuous beam structure correspond to the 18th–34th modes, of which the 25th mode with a frequency of 4966.2 Hz and the 26th mode with a frequency of 4971.4 Hz correspond to the topological edge states, and the rotational angles of the topological state with second-order vibration modes are also localized as shown in Fig. S2(c). The pattern of the third-order vibration modes is similar, and the topological states appear at frequencies 10270 Hz and 10272 Hz. As shown in the blue boxes in Fig. S2(a), the two topological states with first-order vibration modes of the continuous beam structure are within

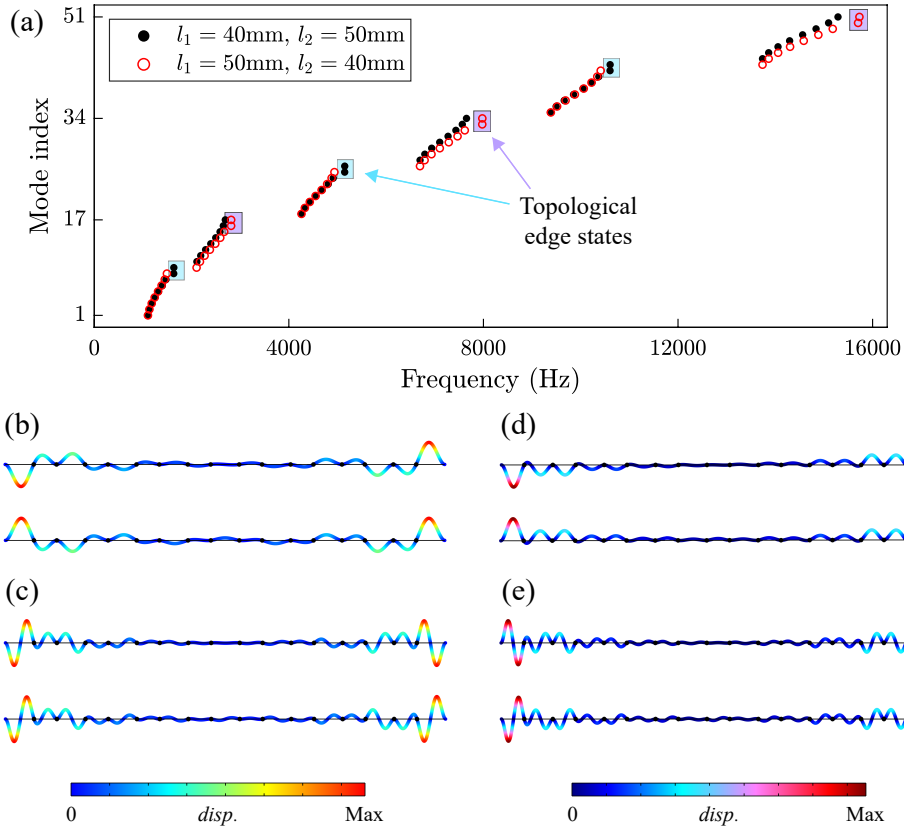


FIG. S2. Numerical results of topological states in continuous beam structure. (a) Comparison of spectra of continuous beam structures with different (interchanged) parameters  $l_1$  and  $l_2$ . The black solid (red hollow) dots represent the spectrum of the continuous beam structure with  $l_1 = 40$  (50) mm and  $l_2 = 50$  (40) mm. (b),(c) Topological states with the first- and second-order mode shapes of the structure with  $l_1 = 40$  mm and  $l_2 = 50$  mm. The maximum absolute values of rotational angles are obtained at the leftmost and rightmost joints. (d),(e) Topological states of the structure with  $l_1 = 50$  mm and  $l_2 = 40$  mm.

the first bandgap, and the two topological states with second-order (third-order) vibration modes appear in the third (fifth) bandgap.

Then, the length intervals of the simple supports in the continuous beam are interchanged and set to  $l_1 = 50$  mm and  $l_2 = 40$  mm, and the natural frequencies of the continuous beam structure are calculated. As shown in Fig. S2(a), the red hollow dots represent the spectrum composed of 51 modes at the lowest frequencies of the structure. The first-order vibration modes of the continuous beam structure correspond to the 1st–17th modes, of which the 16th mode with a frequency of 2353.8 Hz and the 17th mode with a frequency of 2358.2 Hz correspond to the localized topological edge states, shown in Fig. S2(d). The second-order vibration modes of the continuous beam structure correspond to the 18th–34th modes, of which the 33th mode with a frequency of 6578.5 Hz and the 34th mode with a frequency of 6580.7 Hz correspond to the localized topological edge states, shown in Fig. S2(e). The pattern of the third-order vibration modes is similar, and the topological states appear at frequencies 13016 Hz and 13018 Hz. As shown in the purple boxes in Fig. S2(a), the two topological states with first-order vibration modes now appear in the second bandgap, and the two topological states with second-order (third-order) vibration modes appear in the fourth (sixth) bandgap.

### E: Relation of the topological index and Zak phase for continuous beam structure

In this section, we show the rigorous relation between the Zak phase and the topological index which strictly determines the edge states. The solution of rotational angles for eigenequation (C3) is

$$|\theta\rangle = (\theta_A^m, \theta_B^m)^T = \left[ \begin{array}{c} \frac{B(\beta_{l_1})}{A(\beta_{l_1})} + \frac{B(\beta_{l_2})}{A(\beta_{l_2})} \\ \frac{C(\beta_{l_1})}{A(\beta_{l_1})} + \frac{C(\beta_{l_2})}{A(\beta_{l_2})} \cdot e^{ikL} \end{array} \right] = \frac{\sqrt{2}}{2} \left[ \begin{array}{c} 1 \\ e^{i\chi(k)} \end{array} \right], \quad (\text{E1})$$

where  $\chi(k) = \arg \left[ \frac{C(\beta_{l_1})A(\beta_{l_2}) + C(\beta_{l_2})A(\beta_{l_1})e^{ikL}}{B(\beta_{l_1})A(\beta_{l_2}) + B(\beta_{l_2})A(\beta_{l_1})} \right]$ . The Zak phase for each band in Fig. 1(d) is calculated from vector  $|\theta\rangle$  as

$$\gamma = i \int_{-\pi/L}^{\pi/L} dk \langle \theta | \partial_k | \theta \rangle = i \int_{-\pi/L}^{\pi/L} dk \left( \theta_A^{m*} \frac{\partial \theta_A^m}{\partial k} + \theta_B^{m*} \frac{\partial \theta_B^m}{\partial k} \right) = -\frac{1}{2} \chi(k) \Big|_{-\pi/L}^{\pi/L} = -\chi(k) \Big|_0^{\pi/L}. \quad (\text{E2})$$

Due to the inversion symmetry of the continuous beam structure [i.e., if  $(\theta_A^m, \theta_B^m)^T$  is a solution to Eq. (C3), then  $(\theta_B^m, \theta_A^m)^T$  is also a solution to Eq. (C3) with  $k$  inverted], the Zak phase  $\gamma$  is quantized and interpreted as  $\gamma \bmod 2\pi$ . Here we note that the usual definition of the Zak phase [28],

$$\gamma = i \int_{-\pi/L}^{\pi/L} dk \langle \varphi | \partial_k | \varphi \rangle$$

[where  $\varphi(x)$  denotes the Bloch-periodic part of the deflection  $\phi(x)$ ], is in fact equivalent to our expression (E2) which uses  $|\theta\rangle$  and gives identical results. This is due to the fact that the Zak phase of an inversion-symmetric system depends solely on the *product of parities* of the two modes at the center and the boundary of the Brillouin zone,  $k=0$  and  $k=\frac{\pi}{L}$  [34, 35].

For odd-numbered bulk bands,  $B(\beta_{l_1})A(\beta_{l_2}) + B(\beta_{l_2})A(\beta_{l_1})$  is smaller than zero across the whole range of the band (which is straightforward from the analysis of  $\left[ \frac{B(\beta_{l_1})}{A(\beta_{l_1})} + \frac{B(\beta_{l_2})}{A(\beta_{l_2})} \right]$  in Appendix A); thus

$$\chi(k) = \pi + \arg [C(\beta_{l_1})A(\beta_{l_2}) + C(\beta_{l_2})A(\beta_{l_1})e^{ikL}]; \quad (\text{E3})$$

and then, we obtain

$$\chi(0) = \pi + \arg [C(\beta_{l_1})A(\beta_{l_2}) + C(\beta_{l_2})A(\beta_{l_1})] \Big|_{\beta=\beta_b^{(n)}(k=0)}, \quad (\text{E4})$$

where  $\beta = \beta_b^{(n)}(k=0)$  denotes the frequency of the  $n$ -th bulk band when  $k=0$ , and

$$\chi\left(\frac{\pi}{L}\right) = \pi + \arg [C(\beta_{l_1})A(\beta_{l_2}) - C(\beta_{l_2})A(\beta_{l_1})] \Big|_{\beta=\beta_b^{(n)}(k=\frac{\pi}{L})}, \quad (\text{E5})$$

where  $\beta = \beta_b^{(n)}(k=\frac{\pi}{L})$  denotes the frequency of the  $n$ -th bulk band when  $k=\frac{\pi}{L}$ .

For even-numbered bulk bands,  $B(\beta_{l_1})A(\beta_{l_2}) + B(\beta_{l_2})A(\beta_{l_1}) > 0$ ; thus

$$\chi(k) = \arg [C(\beta_{l_1})A(\beta_{l_2}) + C(\beta_{l_2})A(\beta_{l_1})e^{ikL}]. \quad (\text{E6})$$

Therefore, the expression of the Zak phase for odd- and even-numbered bands is unanimously Eq. (E4) minus Eq. (E5), that is, the Zak phases of all frequency bands are obtained as

$$\gamma^{(n)} = \arg [C(\beta_{l_1})A(\beta_{l_2}) + C(\beta_{l_2})A(\beta_{l_1})] \Big|_{\beta=\beta_b^{(n)}(k=0)} - \arg [C(\beta_{l_1})A(\beta_{l_2}) - C(\beta_{l_2})A(\beta_{l_1})] \Big|_{\beta=\beta_b^{(n)}(k=\frac{\pi}{L})}.$$

However, the existence of topological edge states is determined by Eqs. (11) and (12), which is equivalent to evaluating

$$\mu^{(n)} = \arg [C(\beta_{l_1})A(\beta_{l_2}) + C(\beta_{l_2})A(\beta_{l_1})] \Big|_{\beta=\beta_t^{(n)}} - \arg [C(\beta_{l_1})A(\beta_{l_2}) - C(\beta_{l_2})A(\beta_{l_1})] \Big|_{\beta=\beta_t^{(n)}}$$

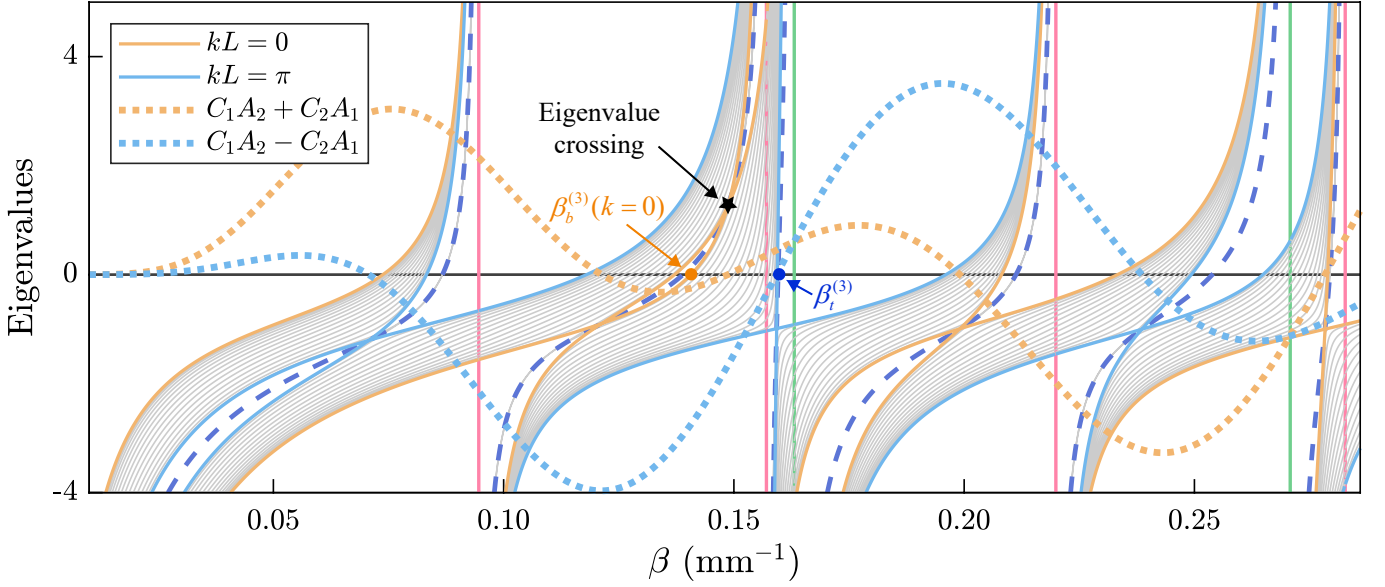


FIG. S3. Eigenvalue spectrum of a periodic continuous beam structure with  $l_1 = 29$  mm, and  $l_2 = 50$  mm, where an “eigenvalue crossing” occurs at a positive eigenvalue (emphasized with a black star); accordingly, function  $[C(\beta l_1)A(\beta l_2) + C(\beta l_2)A(\beta l_1)]$  has opposite signs at  $\beta_t^{(3)}$  and  $\beta_b^{(3)}(k=0)$ . The Zak phase of the third bulk band between frequencies  $(\beta_t^{(2)}, \beta_t^{(3)})$  is  $\pi$ , but no topological states exist at  $\beta_t^{(3)}$  in the third bandgap.

at  $\beta = \beta_t^{(n)}$ ; here the result of  $\pi$  corresponds to Eq. (11) with existent edge states, and 0 corresponds to Eq. (12) without edge states. Thus, the existence of edge states is consistent with the nontrivial Zak phase, if function  $[C(\beta l_1)A(\beta l_2) + C(\beta l_2)A(\beta l_1)]$  has the same sign at  $\beta_t^{(n)}$  and  $\beta_b^{(n)}(k=0)$ , and also function  $[C(\beta l_1)A(\beta l_2) - C(\beta l_2)A(\beta l_1)]$  has the same sign at  $\beta_t^{(n)}$  and  $\beta_b^{(n)}(k = \frac{\pi}{L})$ ; otherwise not. We proceed to give a detailed analysis below with an example structure with  $l_1 = 29$  mm, and  $l_2 = 50$  mm, whose eigenvalue spectrum is shown in Fig. S3.

First, from Eq. (C3), the expressions of eigenvalues for  $H_{\text{Bloch}}^{\text{beam}}$  are

$$\frac{B(\beta l_1)}{A(\beta l_1)} + \frac{B(\beta l_2)}{A(\beta l_2)} \pm \left[ \frac{C(\beta l_1)}{A(\beta l_1)} + \frac{C(\beta l_2)}{A(\beta l_2)} \right] \quad (\text{for } kL = 0), \quad (\text{E7})$$

$$\frac{B(\beta l_1)}{A(\beta l_1)} + \frac{B(\beta l_2)}{A(\beta l_2)} \pm \left[ \frac{C(\beta l_1)}{A(\beta l_1)} - \frac{C(\beta l_2)}{A(\beta l_2)} \right] \quad (\text{for } kL = \pi), \quad (\text{E8})$$

which are represented by orange and blue solid curves in Fig. S3, respectively.

Second, we prove that the expressions of eigenvalues in Eqs. (E7) and (E8) increase monotonically with  $\beta$  (i.e., the orange and blue curves always have positive slopes). It suffices to prove functions  $[\frac{B}{A}(\beta l) + \frac{C}{A}(\beta l)]$  and  $[\frac{B}{A}(\beta l) - \frac{C}{A}(\beta l)]$  always have positive derivatives with respect to its argument  $\beta l$ . We have

$$\left[ \frac{B(\beta l)}{A(\beta l)} + \frac{C(\beta l)}{A(\beta l)} \right]' = \frac{(\cosh \beta l + \cos \beta l + 2)(\cosh \beta l - \cos \beta l - \sinh \beta l \sin \beta l)}{A^2(\beta l)}, \quad (\text{E9})$$

$$\left[ \frac{B(\beta l)}{A(\beta l)} - \frac{C(\beta l)}{A(\beta l)} \right]' = \frac{(\cosh \beta l + \cos \beta l - 2)(\cosh \beta l - \cos \beta l + \sinh \beta l \sin \beta l)}{A^2(\beta l)}. \quad (\text{E10})$$

Because  $\cosh \beta l + \cos \beta l \pm 2 > 0$  for all  $\beta > 0$ , we only need to prove that

$$h_1(x) \equiv \cosh \beta l - \cos \beta l - \sinh \beta l \sin \beta l, \quad (\text{E11})$$

$$h_2(x) \equiv \cosh \beta l - \cos \beta l + \sinh \beta l \sin \beta l \quad (\text{E12})$$

are non-negative. We make the substitutions

$$t \equiv \tan \frac{\beta l}{2}, \quad u \equiv \tanh \frac{\beta l}{2},$$

so that

$$\sin \beta l = \frac{2t}{1+t^2}, \quad \cos \beta l = \frac{1-t^2}{1+t^2}, \quad \sinh \beta l = \frac{2u}{1-u^2}, \quad \cosh \beta l = \frac{1+u^2}{1-u^2};$$

thus, we obtain

$$h_1(x) = \frac{2(u-t)^2}{(1+t^2)(1-u^2)} \geq 0, \quad (\text{E13})$$

$$h_2(x) = \frac{2(u+t)^2}{(1+t^2)(1-u^2)} \geq 0, \quad (\text{E14})$$

which are non-negative, and equal to zero only at discrete points  $u \pm t = 0$  [which are in fact zeros of  $A(\beta l) = \frac{2(t^2-u^2)}{(1+t^2)(1-u^2)}$ ].

Third, the ‘‘eigenvalue crossings’’ (i.e., eigenvalues becoming degenerate) for  $kL = 0$  – represented by intersection points of two orange curves – correspond to the zeros of  $[C(\beta l_1)A(\beta l_2) + C(\beta l_2)A(\beta l_1)]$  (orange dashed line), and those for  $kL = \pi$  – represented by intersection points of two blue curves – correspond to the zeros of  $[C(\beta l_1)A(\beta l_2) - C(\beta l_2)A(\beta l_1)]$  (blue dashed line).

Finally, from the above arguments, we rigorously conclude that when eigenvalue crossing occurs *only at negative values*  $y < 0$ , the existence of topological edge states in the  $n$ -th bandgap is directly determined by the Zak phase of the  $n$ -th bulk band; however, if an eigenvalue crossing occurs *at a positive value*  $y > 0$  in interval  $(\beta_t^{(n-1)}, \beta_0^{n-1})$ , the existence of the topological edge state in the  $n$ -th bandgap is not consistent with the Zak phase, but instead determined by the topological index  $\mu^{(n)}$  defined by Eq. (13):

$$\mu^{(n)} = \gamma^{(n)} + \pi \cdot l^{(n)} \pmod{2\pi},$$

where  $\gamma^{(n)}$  denotes the Zak phase of the  $n$ -th bulk band, and  $l^{(n)}$  is the number of eigenvalue crossings occurring at positive eigenvalues within the frequency range of the  $n$ -th bulk band.

## F: Theoretical framework for general continuum lattice structure

For general continuum lattice structure consisting of intersecting beams, such as bridge-like and kagome frames [Fig. 3(a),(b)], and continuous beams on elastic springs [Fig. 4(a),(b)], the theoretical analysis works in an analogous manner: one takes all joint rotation displacements as basic variables (e.g., represented by  $\theta_i$ ), and the dynamic matrix can be written out in a straightforward manner by following simple rules:

- The  $(i, j)$  nondiagonal entries are  $-\frac{C}{A}(\beta l_{ij})$  (where  $l_{ij}$  denotes the length of beam between two joints  $i$  and  $j$ , if present);
- the  $(i, i)$  diagonal entries are  $\sum_j \frac{B}{A}(\beta l_{ij})$  (where all beam segments around joint  $i$  are taken into account); and
- the remaining entries are left as zero.
- If torsional springs  $k_t$  are present at joints, add  $-\frac{k_t}{\beta EI}$  to the corresponding diagonal entries;
- if elastic foundations  $k_f$  are present at beam segments (e.g., segment between joints  $i$  and  $j$ ), replace  $\frac{B}{A}(\beta l_{ij})$  by  $\frac{\tilde{\beta}}{\beta} \cdot \frac{B}{A}(\tilde{\beta} l_{ij})$  and  $-\frac{C}{A}(\beta l_{ij})$  by  $-\frac{\tilde{\beta}}{\beta} \cdot \frac{C}{A}(\tilde{\beta} l_{ij})$  for those beam segments, where  $\tilde{\beta}$  is defined by  $\tilde{\beta}^4 = \beta^4 - \frac{k_f}{EI}$ .

Such procedure reduces the complex infinite-DOF problem into a small matrix (after performing Bloch analysis) analogous to the Bloch Hamiltonian in finite-DOF topological models. Note that we require all joints to be constrained so as to admit no positional displacements, which is implicitly satisfied by many (but not all) frame structures. This

is because the ratio of the flexural stiffness to the tensile stiffness tends to zero for thin beams. Therefore, flexural motions are predominant rather than longitudinal extensions of beam segments; in other words, for a frame structure, the positions of inner joints may be implicitly constrained as long as the structure has suitable boundary conditions, such as the outermost clamped ends in our examples.

To illustrate the above point, we take the bridge-like frame structure [Fig. 3(a)] as an example. The vector  $|\theta\rangle = (\theta_1, \theta_2, \dots, \theta_{2N-1}, \theta_{2N})^T$  comprises the rotation displacements of the  $2N$  intersection joints of the horizontal beam with all  $2N$  vertical beams (note that all clamped ends, which do not admit rotations, are excluded from  $|\theta\rangle$ ). Then the dynamic matrix  $H^{\text{frame}}$  for the governing equation  $H^{\text{frame}}|\theta\rangle = 0$  of the structure is

$$H^{\text{frame}} = \begin{bmatrix} \sum_{i=0}^2 \frac{B(\beta l_i)}{A(\beta l_i)} & -\frac{C(\beta l_1)}{A(\beta l_1)} & 0 & 0 & \cdots & 0 & 0 & 0 \\ -\frac{C(\beta l_1)}{A(\beta l_1)} & \sum_{i=0}^2 \frac{B(\beta l_i)}{A(\beta l_i)} & -\frac{C(\beta l_2)}{A(\beta l_2)} & 0 & \cdots & 0 & 0 & 0 \\ 0 & -\frac{C(\beta l_2)}{A(\beta l_2)} & \sum_{i=0}^2 \frac{B(\beta l_i)}{A(\beta l_i)} & -\frac{C(\beta l_1)}{A(\beta l_1)} & \cdots & 0 & 0 & 0 \\ 0 & 0 & -\frac{C(\beta l_1)}{A(\beta l_1)} & \sum_{i=0}^2 \frac{B(\beta l_i)}{A(\beta l_i)} & \cdots & 0 & 0 & 0 \\ \vdots & \vdots & \vdots & \vdots & \ddots & \vdots & \vdots & \vdots \\ 0 & 0 & 0 & 0 & \cdots & \sum_{i=0}^2 \frac{B(\beta l_i)}{A(\beta l_i)} & -\frac{C(\beta l_2)}{A(\beta l_2)} & 0 \\ 0 & 0 & 0 & 0 & \cdots & -\frac{C(\beta l_2)}{A(\beta l_2)} & \sum_{i=0}^2 \frac{B(\beta l_i)}{A(\beta l_i)} & -\frac{C(\beta l_1)}{A(\beta l_1)} \\ 0 & 0 & 0 & 0 & \cdots & 0 & -\frac{C(\beta l_1)}{A(\beta l_1)} & \sum_{i=0}^2 \frac{B(\beta l_i)}{A(\beta l_i)} \end{bmatrix},$$

where the functions  $A$ ,  $B$ , and  $C$  are as defined in the main text, and  $l_{0,1,2}$  denote the lengths of beam segments [see Fig. 3(a)]; the corresponding Bloch matrix is then

$$H_{\text{Bloch}}^{\text{frame}} = \begin{bmatrix} \sum_{i=0}^2 \frac{B(\beta l_i)}{A(\beta l_i)} & -\frac{C(\beta l_1)}{A(\beta l_1)} - \frac{C(\beta l_2)}{A(\beta l_2)} e^{-ikL} \\ -\frac{C(\beta l_1)}{A(\beta l_1)} - \frac{C(\beta l_2)}{A(\beta l_2)} e^{ikL} & \sum_{i=0}^2 \frac{B(\beta l_i)}{A(\beta l_i)} \end{bmatrix}.$$

They have an SSH-chain-like form in the subdiagonals, and also the nice property of identical diagonal elements that facilitates our analysis.